



**QUEEN'S  
UNIVERSITY  
BELFAST**

## Order-disorder transition in amorphous vanadium-phosphorus-lithium cathode of lithium ion battery

Kong, F., Sun, D., Rao, Y., Zhang, R., Chen, Z., Wang, D., Yu, X., Jiang, H., & Li, C. (2022). Order-disorder transition in amorphous vanadium-phosphorus-lithium cathode of lithium ion battery. *Applied Surface Science*, 573, Article 151490. <https://doi.org/10.1016/j.apsusc.2021.151490>

**Published in:**  
Applied Surface Science

**Document Version:**  
Peer reviewed version

**Queen's University Belfast - Research Portal:**  
[Link to publication record in Queen's University Belfast Research Portal](#)

### **Publisher rights**

Copyright 2021 Elsevier.

This manuscript is distributed under a Creative Commons Attribution-NonCommercial-NoDerivs License (<https://creativecommons.org/licenses/by-nc-nd/4.0/>), which permits distribution and reproduction for non-commercial purposes, provided the author and source are cited.

### **General rights**

Copyright for the publications made accessible via the Queen's University Belfast Research Portal is retained by the author(s) and / or other copyright owners and it is a condition of accessing these publications that users recognise and abide by the legal requirements associated with these rights.

### **Take down policy**

The Research Portal is Queen's institutional repository that provides access to Queen's research output. Every effort has been made to ensure that content in the Research Portal does not infringe any person's rights, or applicable UK laws. If you discover content in the Research Portal that you believe breaches copyright or violates any law, please contact [openaccess@qub.ac.uk](mailto:openaccess@qub.ac.uk).

### **Open Access**

This research has been made openly available by Queen's academics and its Open Research team. We would love to hear how access to this research benefits you. – Share your feedback with us: <http://go.qub.ac.uk/oa-feedback>

# Order-disorder Transition in Amorphous Vanadium-Phosphorus-Lithium

## Cathode of Lithium Ion Battery

Fanhou Kong<sup>a,b,c</sup>, Dan Sun<sup>b</sup>, Yinzhao Rao<sup>a</sup>, Ruixiang Zhang<sup>a</sup>, Zelin Chen<sup>a</sup>, Dan Wang<sup>a</sup>, Xiaolong Yu<sup>a,c</sup>, Hong Jiang<sup>a,c</sup>, Changjiu Li<sup>a,c,\*</sup>

<sup>a</sup>State Key Laboratory of Marine Resource Utilization in South China Sea (Hainan University)&Special Glass Key Lab of Hainan Province, Haikou, 570228, P. R. China

<sup>b</sup>School of Mechanical and Aerospace Engineering, Queen's University Belfast, Belfast, BT9 5AH, UK

<sup>c</sup>Key Laboratory of Advanced Materials of Tropical Island Resources of Ministry of Education, Haikou, 570228, P. R. China

### \* Corresponding author

**Changjiu Li:** State Key Laboratory of Marine Resource Utilization in South China Sea (Hainan University)&Special Glass Key Lab of Hainan Province, Haikou, 570228, China. E-mail addresses: **lichangjiu@hainanu.edu.cn.**

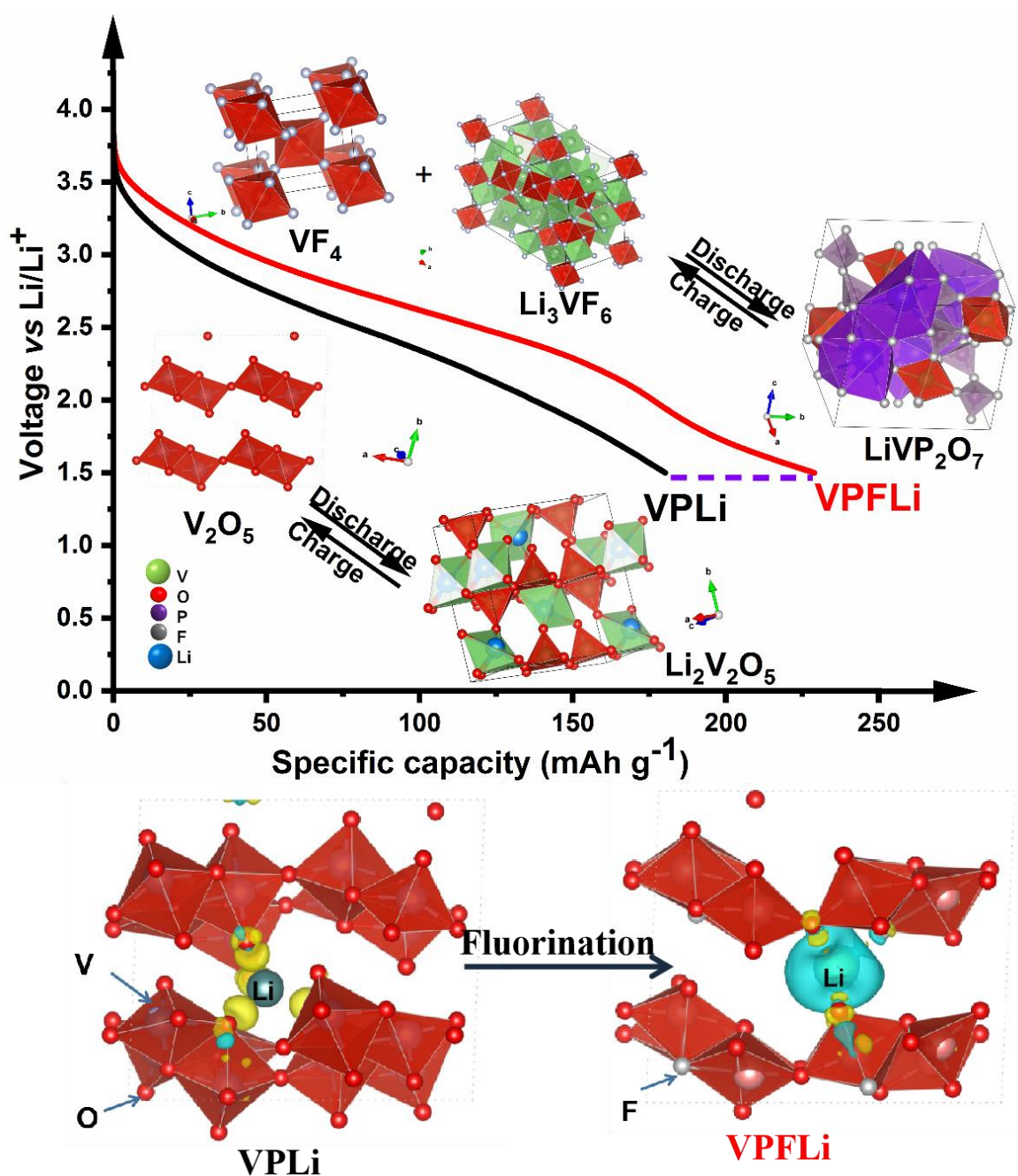
### Highlights

- The effect of fluorination on the order-disorder transition of vanadium-phosphorus-lithium amorphous lithium (VPLi) battery cathode has been investigated for the first time.
- $\text{Li}_3\text{VF}_6$  and  $\text{VF}_4$  nanocrystals were found to precipitate from VPFLi when  $\text{V}^{4+}$  content is ranged from 16.3% to 23.8%.
- $\text{VF}_4$  and  $\text{Li}_3\text{VF}_6$  nanocrystals were converted into  $\text{LiVP}_2\text{O}_7$  in VPFLi, which led to the increased specific capacity of the resulting cathode.
- Density functional theory (DFT) simulation results show that fluorination has led to the movement of Fermi level towards the edge of the conduction band, and the charge transfer from Li to O contributed to the enhanced cycle stability.

### ABSTRACT

Vanadium-based amorphous materials are an emerging category of lithium ion battery cathodes with high specific capacity and high voltage performance. In this study, we investigated the effect of fluorination on the performance of an amorphous vanadium-phosphorus-lithium (VPLi) cathode for lithium ion battery applications. Results show that the fluorinated product consists  $\text{Li}_3\text{VF}_6$  and  $\text{VF}_4$  nanocrystals embedded in an amorphous phase when the  $\text{V}^{4+}$  content was in the range of 16.3% to 23.8%. VPFLi has an optimal

31 specific capacity of  $344.3 \text{ mAh g}^{-1}$  in the first cycle and  $269.7 \text{ mAh g}^{-1}$  after 200 cycles at a current of 50  
 32  $\text{mA g}^{-1}$  within the voltage range of 1.5-4.2V. VPLi has an amorphous structure, and the reversible  $\text{V}^{4+}/\text{V}^{5+}$   
 33 lithiation process corresponds to the conversion between  $\text{V}_2\text{O}_5$  and  $\text{Li}_2\text{V}_2\text{O}_5$  during the charge-discharge  
 34 cycle. Compared to VPLi,  $\text{VF}_4$  and  $\text{Li}_3\text{VF}_6$  crystals were found to convert into  $\text{LiVP}_2\text{O}_7$  in VPFLi, which led  
 35 to the increased specific capacity. Simulation based on density functional theory show that fluorine for  
 36 oxygen has led to the movement of Fermi level moves towards the edge of the conduction band. Charge  
 37 mostly transferred from Li to O which contributed to the improved cathode stability. This study provides a  
 38 new perspective towards selecting novel cathode for lithium-ion batteries.



## 41 **Keywords**

42 Lithium-ion battery; Vanadium; Cathode; Fluorination; Order-disorder transition;

## 43 **1. Introduction**

44 Due to the global energy challenge, low cost and high efficiency energy conversion / storage are  
45 becoming increasingly important in today's society [1-4]. The global energy harvesting system market  
46 accounted for \$449.75 million in 2019 and is expected to reach \$1,097.77 million by 2027 [5]. Lithium ion  
47 batteries are widely used in energy harvesting because of their high specific capacity and cycle stability  
48 [6-9].

49 However, conventional cathode materials such as  $\text{LiFePO}_4$  [10] and NCM (Ni, Co, and Mn) -based  
50 materials [11] suffer from low specific capacity, lack of natural supplies and high cost. Transition metals  
51 (TM), such as vanadium-based compounds [12-14] (e.g.  $\text{V}_2\text{O}_5$  ), are promising alternatives [15] due to their  
52 abundant natural supply source, multivalent states ( $\text{V}^{2+}$ - $\text{V}^{5+}$ ), and high specific capacity [16-19]. However,  
53  $\text{V}_2\text{O}_5$  being an amphoteric acid-base, has limitations such as high dissolution rate, irreversible phase change,  
54 severe volume expansion, and low electronic conductivity [20-22].

55 As a result, many strategies have been explored to improve the performance of vanadium-based electrode  
56 materials, such as deploying multi-dimensional structures [18,23,24], disordered rock salt [25-29],  
57 conductive coating [30-33], valence transition [34-38], and phase transformation [39-41], etc.

58 However, in contrast to the mature crystalline based lithium battery electrode material technologies, the  
59 performance and working mechanism of amorphous electrode materials are far less understood. In recent  
60 years, amorphous glass materials [42-44] have received increasing attention in lithium battery electrode  
61 development. Y. Zhang and Y. Yue et al [45] explored the structural factors that affect the electrochemical  
62 performance of glass anodes, especially the structural evolution during the discharge-charge process. In a  
63 separate study, they [46] found that the structural network of the electrode can be dissociated into isolated  
64 units through solid-state nuclear magnetic resonance, and form different types of highly ordered

65 nano-domains, which led to favorable rate capability and long-term cycle stability. H. Tao and Y. Yue et al  
66 [47] succeeded in tuning the degree of disorder in NaFePO<sub>4</sub> cathode material by a mechanochemical route,  
67 thereby obtaining the excellent cycling stability. To date, applications of vanadium oxide-based amorphous  
68 glass electrode materials have been reported by several research groups, examples include  
69 vanadium-phosphorus [48-50], vanadium-boron [51], vanadium-tellurium [52-54], and  
70 vanadium-silicon[55], etc. Due to the lack of accurate *in situ* characterization for amorphous electrode  
71 structure, the current research mostly focus on the composition-performance improvement, and the results  
72 cannot track the cycle process, reveal the lithiation mechanism, or support theoretical calculations.

73 Oxygen pairs, short-range O-O bonds and the formation of oxygen vacancies can lead to the voltage  
74 drop and capacity degradation during long term cycling of the cathode [56]. Due to the greater  
75 electronegativity of F (4.0) as compared to O (3.5), F has a stronger ability to attract electrons. In this work,  
76 we reported the first study on fluorine-oxygen substitution in an amorphous lithium-ion battery cathode  
77 system. An amorphous vanadium-phosphorus-lithium cathode material (VPLi) and its fluorinated product  
78 (VPFLi) were prepared by melting quenching method. Specifically, the thermodynamic properties of both  
79 materials were characterized to reveal the difference in their lithiation mechanisms. This is followed by  
80 detailed evaluation using DSC, *in situ* XRD, FT-IR, Raman, SEM, TEM, NMR, XPS, and EPR. The order  
81 /disorder phase transformation in the fluorinated amorphous electrode material were revealed. The cathode  
82 materials electrochemical properties, including their specific capacity, rate performance, long-term cycling,  
83 have been assessed and compared using a practical lithium-ion battery cell set up. Finally, DFT calculations  
84 were performed to reveal the difference in the charge density distribution between the electrode materials  
85 with and without fluorination.

## 86 **2. Methodology**

### 87 **2.1. Materials Preparation**

88 Amorphous vanadium-phosphorus-lithium cathode materials with and without fluorine-oxygen  
89 substitution were prepared by melting-quenching method [48]. VPLi was prepared by mixing raw materials

90  $\text{Li}_3\text{PO}_4$  (Macklin, CP, 99.0%) /  $\text{V}_2\text{O}_5$  (Macklin, AR, 99.99%) with a molar ratio of 4:6, using a vertical mixer  
91 for 30 min. The mixture was placed into an alumina crucible, heated in a tube furnace under Ar atmosphere  
92 to 700 °C at a rate of 10 °C/min. The temperature was maintained at 700 °C for 30 min and then raised to  
93 900 °C for another 10 min of heating. The end of the tube furnace is connected to the quenching box  
94 (30cm\*30cm\*30cm). The resulting molten liquid was passed between two copper plates and quenched in Ar  
95 to room temperature to obtain a shaped glass specimen. The glass specimen was then annealed at 225 °C for  
96 400 min to relieve the residual stresses and was cooled down to room temperature naturally. The glass  
97 specimen was ground into glass powder (particle size < 10  $\mu\text{m}$ ) and the resultant amorphous material was  
98 named as VPLi. For fabrication of fluorinated VPFLi, a mixture of  $\text{Li}_3\text{PO}_4$  (Macklin, CP, 99.0%),  $\text{V}_2\text{O}_5$   
99 (Macklin, AR, 99.99%) and LiF (Macklin, AR, 99.0%) with a molar ratio of 3:6:3 were used and the  
100 preparation process of VPFLi is the same as that of VPLi. The material preparation process is shown in  
101 Fig.1.

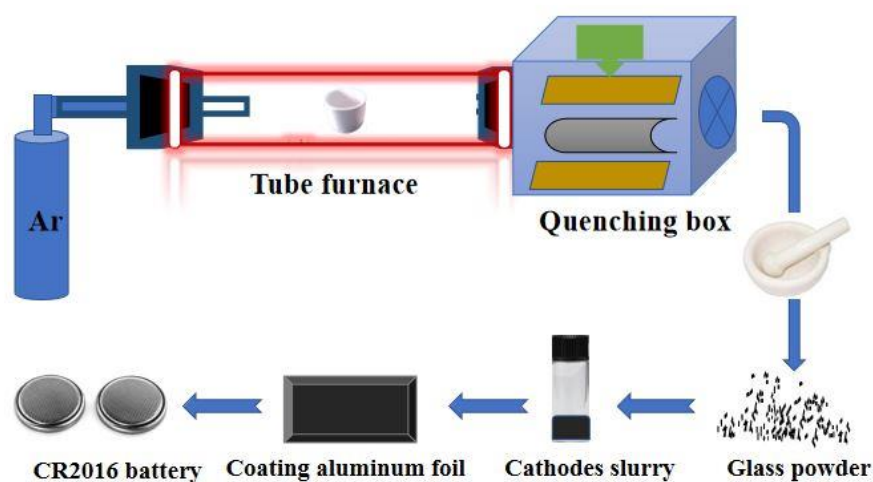
## 102 2.2. Characterization

103 Differential scanning calorimetry (DSC, NETZSCH STA449) was conducted to study the materials  
104 thermodynamic parameters under  $\text{N}_2$ , with a heating rate of 10 °C/min. X-ray diffractometry (XRD, Rigaku,  
105 smartlab 9kw) and *in situ* high and low temperature XRD (Rigaku TTR3) were used to identify the materials  
106 crystal structures. Fourier Transform infrared spectroscopy (FT-IR, Thermo fisher Nicolet iS5) and Raman  
107 spectroscopy (HORIBA Scientific HORIBA LabRAM HR Evolution) using a laser Raman spectrometer  
108 from Renishaw plc (532 nm) were performed. Microstructure analysis was carried out by transmission  
109 electron microscopy (TEM, JEOL JEM-2100F) and scanning electron microscopy (SEM, Verios G4 UC)  
110 with an energy dispersive spectrometer (EDS, Oxford Instruments). NMR measurements of  $^{19}\text{F}$  were  
111 performed by a 600 MHz SS-NMR spectrometer JEOL ECZ600R/S3 equipped with a 14.09 T  
112 superconducting magnet and a 3.2mm double-resonance MAS probe (JEOL RESONANCE Inc., Japan).  
113 Particle size distribution was measured by a zetasizer nano ZS90 (Malvern Instrument). X-ray photoelectron  
114 spectroscopy (XPS, AXIS Supra) with  $\text{MgK}\alpha$  excitation source was used to detect the relative V content in

115 different valence states and the different coordination of O. The electron paramagnetic resonance (EPR,  
116 Bruker A320) was used to detect the unpaired electrons in the atoms or molecules to explore the structural  
117 characteristics of its surrounding environment.

### 118 2.3. Electrochemical measurements

119 Two different cathodes were prepared by mixing conductive carbon black (super P) and polyvinylidene  
120 fluoride (PVDF) binder with VPLi and VPFLi, respectively, at a mass ratio of 7:2:1. N-methyl pyrrolidone  
121 (NMP) (15 wt%) was added, and the mixture was ground into a slurry. The slurry was coated onto an  
122 aluminum foil, dried thoroughly under vacuum condition, and cut into 10 mm diameter disks to be used as  
123 the cathode. CR2016 type coin cells were assembled with lithium being the anode, Celgard 2025 being the  
124 separator, and an electrolyte containing 1.0 M LiPF<sub>6</sub> in ethylene carbonate (EC), dimethyl carbonate (DMC),  
125 and ethyl methyl carbonate (EMC) with a volume ratio of 1:1:1. The entire assembly was completed in a  
126 vacuum glove box filled with Ar (H<sub>2</sub>O and O<sub>2</sub> content <1 ppm). The preparation process is shown in Fig.1.  
127 Battery cycling (Land CT3001A) was conducted at a constant current of 0.1A g<sup>-1</sup> and 50 mA g<sup>-1</sup> to study the  
128 cycling behaviour and rate capability within a voltage range of 1.5–4.2 V. Cyclic voltammetry (CV) was  
129 performed on an electrochemical workstation (CHI660E) in a voltage range of 1.5–4.2 V, at a scan rate of  
130 0.5 mV/s. CHI660E was used to perform electrochemical impedance spectroscopy (EIS) in a frequency  
131 range of 10<sup>-2</sup>–10<sup>5</sup> Hz, at an amplitude of 5 mV.



132  
133 Fig.1 Schematic diagram of the material preparation process

### 3. Results and discussion

#### 3.1 Structure and thermodynamic properties of fluorination on VPLi

DSC results in Fig.2(a) shows that the glass transition temperature ( $T_g$ ) of VPLi was 224 °C, with three crystal precipitation temperatures ( $T_C$ ), 259 °C ( $T_{C1}$ ), 329 °C ( $T_{C2}$ ) and 474 °C ( $T_{C3}$ ) and a melting temperature ( $T_m$ ) of 569 °C ( $T_{m1}$ ). The  $T_g$  of VPFLi was found to be 220 °C, with  $T_{C1}$  and  $T_{C2}$  being 239 °C and 489 °C, respectively, and  $T_{m1}$ ,  $T_{m2}$  and  $T_{m3}$  being 349 °C, 409 °C and 545 °C, respectively. The lower  $T_C$  of VPFLi as compared to VPLi suggests the lower activation energy of the crystallization process required for the fluorinated system. Compared with VPLi, VPFLi has fewer crystallization peaks and more melting peaks, indicating multiple crystal systems are present in the system.

VPLi was heated and studied *in situ* using high and low temperature XRD, as shown in Fig.2(b). The sample (VPLi-25 °C) was first heated to 270 °C at a rate of 10 °C /min and held for 30 min (VPLi-270 °C), followed by heating to 340 °C at a rate of 10 °C /min, and maintained for 30 min (VPLi-340 °C). Finally, the material was cooled down to room temperature naturally (VPLi-C25 °C). Fig.2(b) shows that VPLi-25 °C has an amorphous phase, at elevated temperatures, VPLi-270 °C showed the precipitation of crystalline  $\text{Li}_3\text{P}$  (PDF#04-0525), and VPLi-340 °C showed precipitation of crystalline  $\text{Li}_{0.3}\text{V}_2\text{O}_5$  (PDF#18-0755). The fact that VPLi possesses two potential crystal precipitation pathways suggests the material is in a thermodynamically metastable state and different heat treatment conditions can lead to precipitation of either crystalline  $\text{Li}_3\text{P}$  or  $\text{Li}_{0.3}\text{V}_2\text{O}_5$ . Fig.2(c) compares the XRD pattern of VPLi and VPFLi at room temperature (25 °C). Compared to the neat amorphous VPLi, VPFLi showed ordered crystalline precipitation of  $\text{VF}_4$  (PDF#19-1409) and  $\text{Li}_3\text{VF}_6$  (PDF#28-0607).

Fig.2(d) shows the FT-IR spectra of VPLi, VPFLi, and as purchased  $\text{Li}_3\text{PO}_4$ , and  $\text{V}_2\text{O}_5$ . The characteristic absorption peak at 1624  $\text{cm}^{-1}$  represents the stretching vibration of  $\text{V}=\text{O}$ . The absorption band at 1010  $\text{cm}^{-1}$ , represents the tensile vibration of the  $\text{V}^{5+}=\text{O}$  bond [57] of VPLi, VPFLi and  $\text{V}_2\text{O}_5$ . The characteristic absorption peak at 1030  $\text{cm}^{-1}$  represents the asymmetric stretching vibration of the tetrahedron  $[\text{PO}_4]$  [58]. The characteristic peaks at 946  $\text{cm}^{-1}$  and 922  $\text{cm}^{-1}$  can be correlated to the asymmetric vibration of P-O-P



[58]. of the red shift of P-O-P can be attributed to the presence of F [59].

In the subsequent Raman analysis (Fig.2(e)), the peaks at 287 and 538  $\text{cm}^{-1}$  seen in VPLi and VPFLi can be attributed to the bending mode of the V-O-V bond [18]. Characteristic peaks such as 766 and 990  $\text{cm}^{-1}$  are related to the tensile vibrations of the double-coordinated oxygen ( $\text{V}_2\text{-O}$ ) and vanadium oxide ( $\text{V=O}$ ) [18].  $\delta^{19}\text{F}$  frequency-stepping spectra (Fig.2(f)) obtained from solid-state NMR of VPFLi exhibited strong signals and chemical shifts which can be referenced against fluorotrichloromethane ( $\text{CCl}_3\text{F}$ ,  $\delta(^{19}\text{F}) = 0 \text{ ppm}$ ) [26]. However, no such signal has been found in VPLi in this region [46].

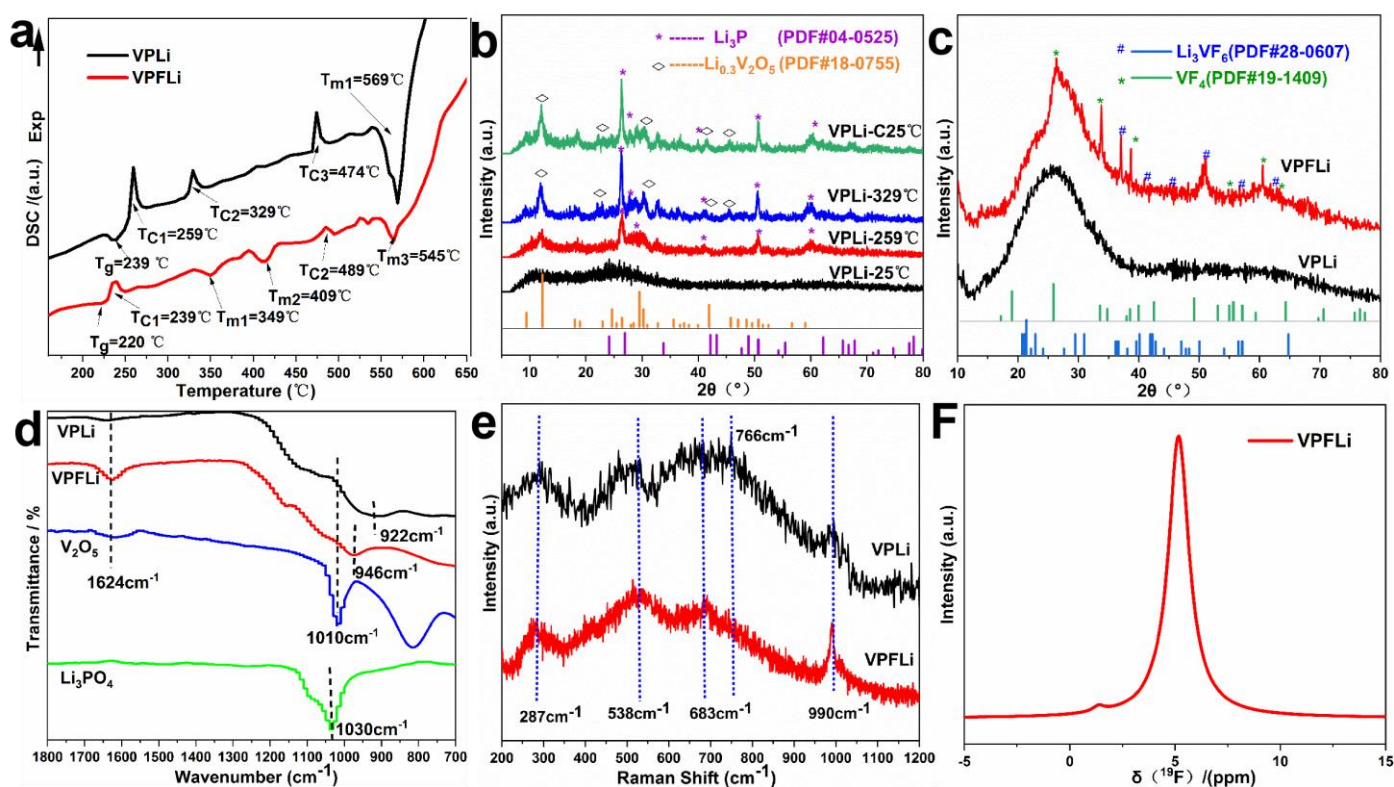
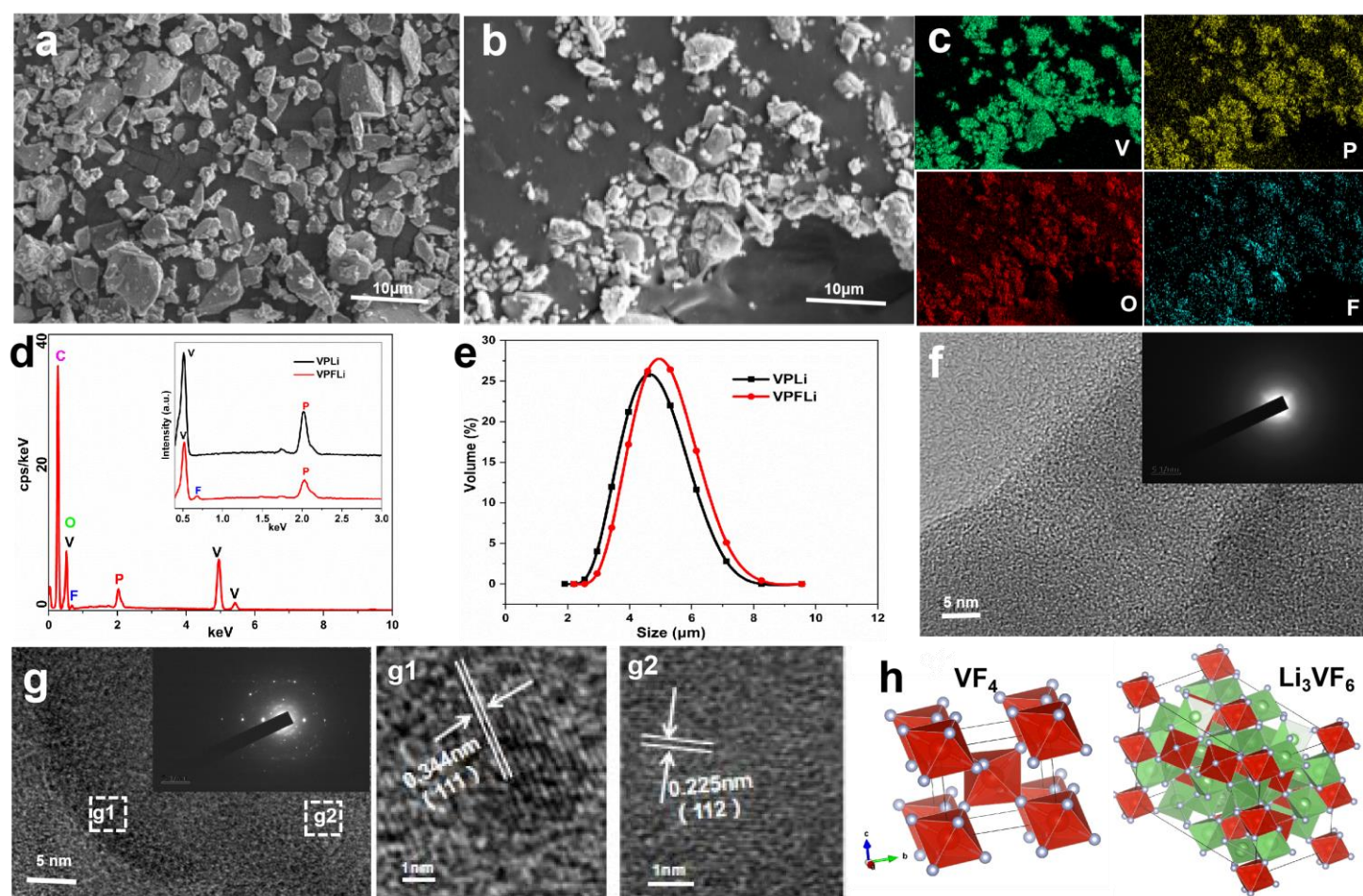


Fig.2. (a) DSC scan of VPLi and VPFLi, (b) *in situ* XRD pattern of VPLi at different temperatures, (c) XRD pattern of VPLi and VPFLi, (d) IR spectra of VPLi, VPFLi,  $\text{Li}_3\text{PO}_4$ , and  $\text{V}_2\text{O}_5$ , (e) Raman spectra of VPLi and VPFLi, and (f)  $^{19}\text{F}$  frequency-stepping spectra of VPFLi obtained by solid-state NMR.

SEM images of VPLi and VPFLi are shown in Fig.3(a)-(b). Elements V, P, O and F within VPFLi were identified in the EDS elemental mapping and its associated spectra Fig.3(c)-(d). EDX point analysis confirms the substitution molar ratio of fluorine for oxygen is 1:10. The particle sizes of VPLi and VPFLi are in the range of 2-10  $\mu\text{m}$  according to the analysis using , Fig.3(e). Since  $\text{F}^{-1}$  ion has a smaller radius (0.133nm) than  $\text{O}^{2-}$  (0.136nm), it is less prone to the concentration quenching effect [60], and can render a higher doping concentration. The TEM images and the associated SAED patterns suggest VPLi (Fig.3(f))

176 has a disordered amorphous structure. In contrast, VPFLi (Fig3(g)) features nano-polycrystals embedded in  
 177 an amorphous phase, which corroborate well with the previous XRD pattern (Fig.2(c)). The insets shown in  
 178 Fig.3(g1)-(g2) confirm the presence of nanocrystalline regions in VPFLi. The interplanar lattice spacing of  
 179 0.344 nm and 0.225 nm correspond to the (111) plane of  $\text{VF}_4$  (PDF#19-1409) nanocrystal and (112) plane of  
 180  $\text{Li}_3\text{VF}_6$  (PDF#28-0607) nanocrystal, respectively. Fig.3(h) shows the crystal structures of  $\text{VF}_4$  and  $\text{Li}_3\text{VF}_6$ ,  
 181 respectively.



182

183 Fig.3. Microstructure and elemental analysis of VPLi and VPFLi. (a) SEM of VPLi, (b) SEM of VPFLi, (c) elemental  
 184 mapping of VPFLi, (d) EDS of VPFLi (insets: comparison between VPLi and VPFLi), (e) Particle size distribution of VPLi  
 185 and VPFLi, (f) TEM of VPLi with SAED pattern, (g) TEM of VPFLi with SAED pattern (insets: lattice structure of (g1)  
 186 (111) plane of  $\text{VF}_4$  and (g2) (112) plane of  $\text{Li}_3\text{VF}_6$ ), (h) the crystal structure of  $\text{VF}_4$  and  $\text{Li}_3\text{VF}_6$ .

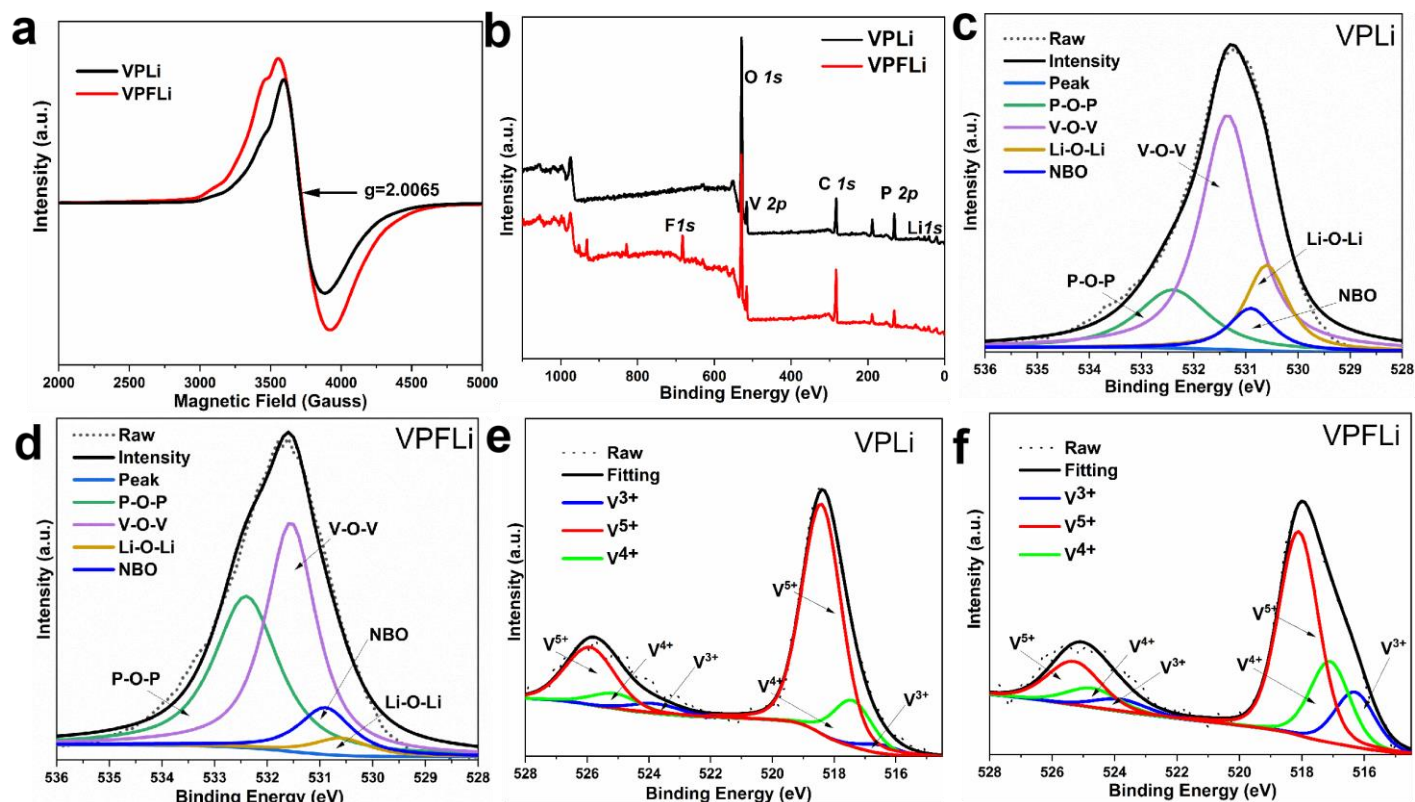
187

Vanadium usually presents in  $\text{V}^{5+}$ ,  $\text{V}^{4+}$ , and  $\text{V}^{3+}$  states in vanadate glass with their respective electronic  
 188 structures  $3p^63d^0$ ,  $3p^63d^1$ , and  $3p^63d^2$ . The electron paramagnetic resonance is an effective technique for  
 189 detecting  $\text{V}^{4+}$  [61] as the unpaired electrons surrounding the  $\text{V}^{4+}$  nucleus can generate strong EPR signals.

190 VPLi and VPFLi have the same stoichiometry during the test. Fig.4(a) shows that the EPR peak intensity of  
191 VPFLi is ~ 1.46 times greater than that of VPLi, confirming the significantly increased V<sup>4+</sup> content in  
192 VPFLi.

193 The full spectrum XPS survey (Fig.4(b)) shows that VPFLi contains V2p, P2p, O1s, Li1s, C1s and F1s,  
194 and VPLi contains V2p, P2p, O1s, Li1s and C1s. The relative abundance of P-O-P, V-O-V, Li-O-Li and  
195 non-bridging oxygen (NBO) can be found from the high-resolution O1s XPS spectra in Fig.4(c) (VPLi),  
196 Fig.4(d) (VPFLi) and Table 1. After fluorination, O1s of the V-O-V bonds (531.3 eV) reduced significantly  
197 from 56.7% to 46.9% and the Li-O-Li bonds (530.6 eV) reduced from 16.2% to 3.9%. This is because, the  
198 Li-O-Li structure can induce non-hybridization of the oxygen atomic orbital. The orbital energy level is  
199 raised to a level between the transition metal e<sub>g</sub>\* and t<sub>2g</sub> levels, which induces the redox reaction of oxygen  
200 [56] and triggers the V-F bond formation. In contrast, O1s of the P-O-P bonds (532.4 eV) increased  
201 significantly from 3.0% to 16% and the NBO bonds (530.9 eV) increased from 8.3% to 10%.

202 As shown in Fig.4 (e) and (f), the peak position of the V 2p<sub>3/2</sub> XPS spectra at 516.5 eV can be assigned  
203 to V<sup>3+</sup>, 517.4 eV to V<sup>4+</sup>, and 518.1 eV to V<sup>5+</sup> [48.62] in VPLi and VPFLi. Literature [63] reports that V<sup>4+</sup>  
204 content is related to electrical conductivity. Table 2 shows that after fluorination, V<sup>3+</sup> content increased from  
205 3.0% to 16.2%, and the V<sup>4+</sup> content increased from 16.3% to 23.8% with the V<sup>5+</sup> content decreased from  
206 80.7% to 60.0%, indicating effect of fluorination in reducing the valence state of V. As such, Li<sub>3</sub>VF<sub>6</sub> can be  
207 considered as an emerging electrochemically active lithium intercalation material [64]. In Li<sub>3</sub>VF<sub>6</sub>, the  
208 substitution of O by F leads to reduced overall number of negative charges. To maintain the material's  
209 electrical neutrality, the average valence of V must decrease, which can be achieved by V<sub>2</sub>O<sub>5</sub> to V<sub>2</sub>O<sub>4</sub> / V<sub>2</sub>O<sub>3</sub>  
210 conversion during heating of VPLi [65]. From Table 2, it can be seen that the lower valence V is dominated  
211 by V<sub>2</sub>O<sub>4</sub> and with the greater number of V<sup>4+</sup> participating in the electrode reaction (V<sup>4+</sup>/V<sup>3+</sup>), the electrode's  
212 discharge capacity is expanded accordingly. In addition, V<sub>2</sub>O<sub>4</sub> has a unique structure consisting of [VO<sub>6</sub>]  
213 octahedral double layers connected by shared corners, which provides efficient diffusion paths for Li<sup>+</sup> ions



215

216 Fig.4. EPR and XPS spectra of VPLi and VPFLi: (a) EPR spectrum survey, (b) XPS full spectrum survey, (c) *O* 1s  
 217 deconvolution for VPLi, (d) *O* 1s deconvolution for VPFLi, (e) *V* 2p deconvolution for VPLi, (f) *V* 2p deconvolution  
 218 for VPFLi.

219 Table 1 Relative abundance of P-O-P, V-O-V, Li-O-Li and NBO obtained from high-resolution *O* 1s XPS spectra.

	P-O-P		V-O-V		Li-O-Li		NBO		FWHM (eV)	Lorenz-Gaussian ratio(%)
	Main peak(eV)	Area (%)	Main peak(eV)	Area (%)	Main peak(eV)	Area (%)	Main peak(eV)	Area (%)		
VPLi	532.4	18.8	531.3	56.7	530.6	16.2	530.9	8.3	1.25	80
VPFLi		39.2		46.9		3.9		10		

220

221 Table 2 Relative abundance of V obtained from high-resolution *V* 2p<sub>3/2</sub> / (*V* 2p<sub>1/2</sub>) XPS spectra.

	V <sup>3+</sup>		V <sup>4+</sup>		V <sup>5+</sup>		FWHM (eV)	Lorenz-Gaussian ratio(%)
	Main peak(eV)	Area (%)	Main peak(eV)	Area (%)	Main peak(eV)	Area (%)		
VPLi	516.5/(523.8)	3.0	517.4/(524.7)	16.3	518.1/(525.4)	80.7	1.5/(2)	80
VPFLi		16.2		23.8		60.0		

222

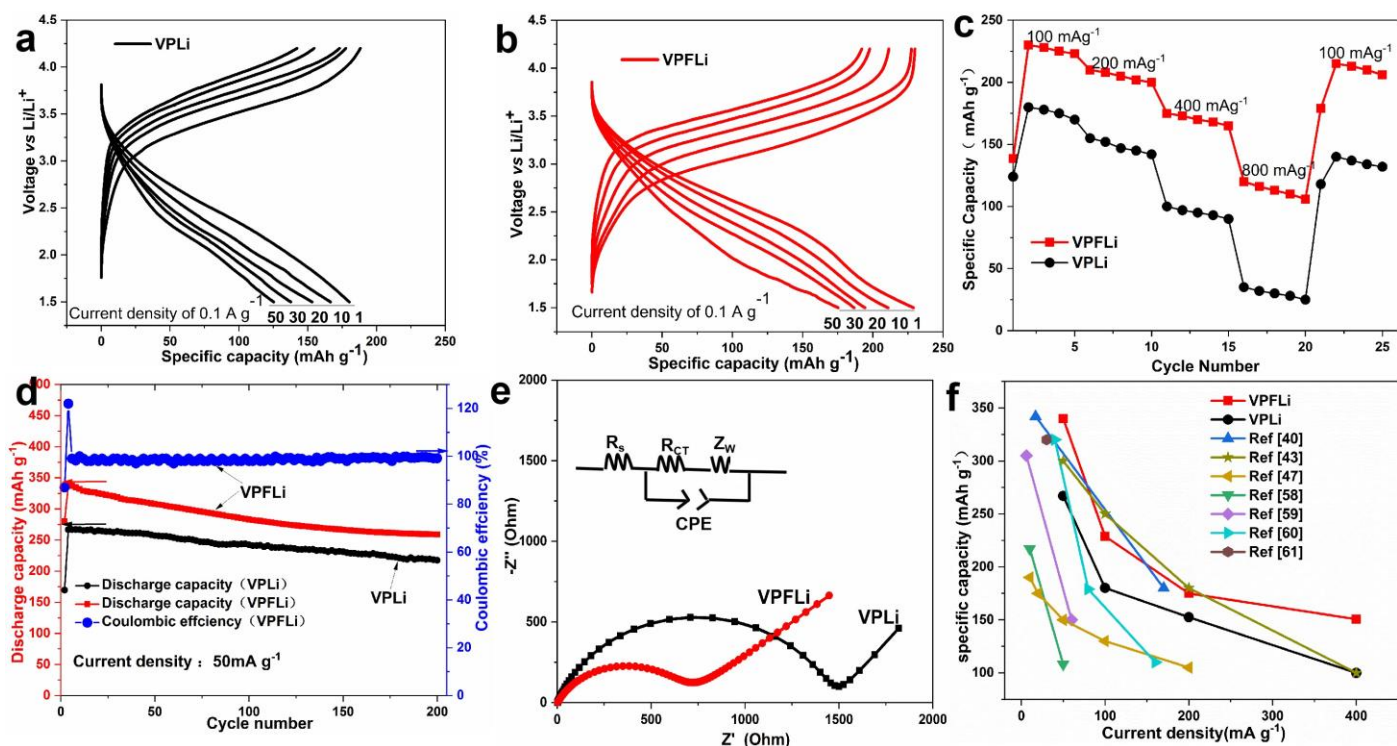
### 3.2 Characterization of battery electrochemical performance

The electrochemical performance of CR2016 type coin cells was studied in detail. As shown in Fig.5(a), VPLi provided specific capacities of 180.1, 166.4, 153.2, 137.7 and 125.3 mAh g<sup>-1</sup> for the 1<sup>st</sup>, 10<sup>th</sup>, 20<sup>th</sup>, 30<sup>th</sup>, and 50<sup>th</sup> cycle, respectively, under a current density of 0.1A g<sup>-1</sup>, within a voltage range of 1.5 - 4.2V. In contrast, VPFLi (Fig.5(b)) presented enhanced specific capacities of 228.9, 210.8, 193.5, 186.7 and 174.7 mAh g<sup>-1</sup> for the same cycles, under the same conditions. After 50 cycles, the specific capacity retention rates were 76.3% for VPFLi and 69.6% for VPLi, respectively. Fig.5(c) gives the rate performance of the VPLi and VPFLi under various current densities (100, 200, 400, 800 and 100 mA g<sup>-1</sup>). The discharge capacities of VPLi were 185–173, 157–142, 95–76, 30–19 and 145–135 mAh g<sup>-1</sup>, respectively and for VPFLi, greater discharge capacities have been observed (228–220, 208–198, 179–165, 120–99 and 210–205 mAh g<sup>-1</sup>, respectively) under the same testing conditions.

According to the long-term cycling results shown in Fig.5(d), VPLi presented optimal capacities of 266.8 mAh g<sup>-1</sup>, and 197.6 mAh g<sup>-1</sup> after 200 cycles at a current density of 50 mA g<sup>-1</sup> with capacity retention rate 74.0%. VPFLi presented greater optimal capacities of 344.3 mAh g<sup>-1</sup>, and 269.7 mAh g<sup>-1</sup> after 200 cycles with the coulombic efficiency approaching 100%, at a current density of 50 mA g<sup>-1</sup> with capacity retention rate 78.3%. The result implies that VPFLi is a promising material for reversible Li<sup>+</sup> storage. Due to the greater electronegativity of F (4.0) as compared to O (3.5), it has a stronger ability to attract electrons, and its resulting covalent bonding strength with V is higher. V-F covalent bond helps to maintain a stable crystal structure during repeated charge/discharge processes, and effectively improves the cycle stability of the VPFLi.

The electrical conductivity of the assembled battery was evaluated by EIS [18]. Fig.5(e) shows that the charge transfer resistance of VPFLi ( $R_{CT} = 704 \Omega$ ) was only half that of VPLi ( $R_{CT} = 1499.7\Omega$ ). This suggests that substituting F for O of VPFLi and the associated increased V<sup>4+</sup> content can improve the electrical conductivity of the electrode and hence enhance its rate performance. Fig.5 (f) compares the specific capacity values of VPLi and VPFLi with other cathode materials reported in the literature. In

248 general, the capacity performance of VPFLi is better (particularly at low and high current densities) than the  
 249 existing amorphous vanadium-based cathode materials, such as  $\text{H}_2\text{-V}_2\text{O}_5\text{-P}_2\text{O}_5$  [48],  $\text{V}_2\text{O}_5\text{-LiBO}_2$   
 250 [51],  $\text{Li}_2\text{O-V}_2\text{O}_5\text{-SiO}_2\text{-B}_2\text{O}_3$  [66],  $\text{C-Li}_2\text{O-V}_2\text{O}_5\text{-P}_2\text{O}_5$  [67],  $\epsilon\text{-VOPO}_4$  [68], and vanadium-based crystal  
 251 cathode materials  $\text{V}_2\text{O}_5$  nanofibers [69],  $\text{V}_2\text{O}_5$  nanoribbon [70].



252

253 Fig.5. Electrochemical performance of VPLi and VPFLi. (a)-(b) Galvanostatic charge and discharge profiles of VPLi and  
 254 VPFLi at a current density of  $0.1 \text{ A g}^{-1}$ , (c) Rate performance of VPLi and VPFLi, (d) Long-term cycling of VPFLi, (e) EIS  
 255 measurements of VPLi and VPFLi, (f) Comparison of specific capacities with reported cathode materials in the literature.

256

### 3.3 Lithiation mechanism and DFT calculations

257

258

259

260

261

262

263

264

265

Fig.6(a) shows the CV curves of VPLi and VPFLi at a scan rate of  $0.5 \text{ mV/s}$ . For VPLi, the peaks at  $1.2 \text{ V} / 0.6 \text{ V}$  and  $3.5 \text{ V} / 3.8 \text{ V}$  can be associated with the redox reaction processes  $\text{V}^{4+}/\text{V}^{5+}$  due to the extraction and insertion of  $\text{Li}^+$  [71.72]. The broad peaks at  $1.7 \text{ V}$  and  $2.6 \text{ V}$  seen for VPFLi can be associated with the redox reaction processes  $\text{V}^{3+}/\text{V}^{4+}$  [68]. Fig.6(b) - (c) shows the *ex situ* XRD spectra of VPLi and VPFLi at different stages of the first charge /discharge cycle at a current rate of  $200 \text{ mA g}^{-1}$ , *i.e.*, in the initial state (OCV,  $3 \text{ V}$ ),  $1.2$  ( $2.6$ )  $\text{V}$  (discharge),  $0.01 \text{ V}$  (discharge),  $0.6$  ( $1.7$ )  $\text{V}$  (charge),  $3.5 \text{ V}$  (charge), and  $3 \text{ V}$  (discharge). As shown in Fig.6(b), nanocrystal  $\text{Li}_2\text{V}_2\text{O}_5$  (PDF#48-0076) precipitation within VPLi can be signified by the characteristic peaks at  $0.6 \text{ V}$  (charge) and  $3.5 \text{ V}$  (charge). These peaks subsequently disappeared at  $3.0 \text{ V}$  (discharge) in the first cycle of VPLi. In contrast,  $\text{LiVP}_2\text{O}_7$  (PDF#46-0311) and  $\text{Li}_2\text{V}_2\text{O}_5$  (PDF#48-0076)

266 nanocrystals precipitation was found for VPFLi at 1.7 V (charge) and 3.5 V (charge), which subsequently  
267 disappeared at 3.0 V (discharge) in Fig.6(c).

268 The TEM image of VPLi at 3.5 V (charge) in the first cycle (Fig.6(d)) confirms the material is in a single  
269 crystal  $\text{Li}_2\text{V}_2\text{O}_5$  state. The inter-planar distance of 0.281 nm in Fig (d1) further confirms it is correlated to the  
270 (112) plane of  $\text{Li}_2\text{V}_2\text{O}_5$  (PDF#48-0076). The theoretical specific capacity of the  $\text{V}_2\text{O}_5$  electrode with one  $\text{Li}^+$   
271 inserted is  $147 \text{ mAh g}^{-1}$  and that with two  $\text{Li}^+$  inserted is  $294 \text{ mAh g}^{-1}$  [16]. The specific capacity of VPLi  
272 has an intermediate value ( $180 \text{ mAh g}^{-1}$ ), see Fig.5(a), which indicates the associated  $\text{V}^{4+}/\text{V}^{5+}$  lithiation  
273 process involves conversion of  $\text{V}_2\text{O}_5$  into  $\text{Li}_2\text{V}_2\text{O}_5$  in the first cycle of VPLi [22.73].

274 On the other hand, the TEM image in Fig.6(e) shows that VPFLi at 3.5 V (charge) is in a polycrystalline  
275 state in the first cycle. Fig.(e1) shows the inter-planar distance of 0.656 nm corresponds to the (001) plane of  
276  $\text{LiVP}_2\text{O}_7$  (PDF#46-0311. Fig.(e2) shows the inter-planar lattice spacing of 0.323 nm corresponds the (103)  
277 plane of  $\text{Li}_2\text{V}_2\text{O}_5$  (PDF#48-0076). These results corroborate well with the XDR data in Fig.6(c). Addition of  
278  $\text{LiVP}_2\text{O}_7$  is known to improve the electrode materials capacity and rate performance [74.75], as it can  
279 generate a series of V-based multiple redox couples, which offers additional active locations for  $\text{Li}^+$  ion  
280 storage and effectively shortens the  $\text{Li}^+$  ion diffusion pathway.  $\text{Li}^+$  is stored in the channel formed by the  
281 corner-sharing  $[\text{VO}_6]$  octahedron and the  $\text{P}_2\text{O}_7$  group, which is coordinated by four oxygen atoms in the  
282  $\text{LiVP}_2\text{O}_7$  crystal structure [76]. The volume of VPLi and VPFLi remain constant during the  $\text{Li}^+$  insertion or  
283 extraction process (no significant peak shift in XRD spectra). The reversible peak position and peak  
284 intensity in the XRD pattern of VPLi and VPFLi during the charge-discharge cycle indicate both materials  
285 are intercalation-type lithium storage materials[77]. The reaction mechanism is shown in Fig.7.

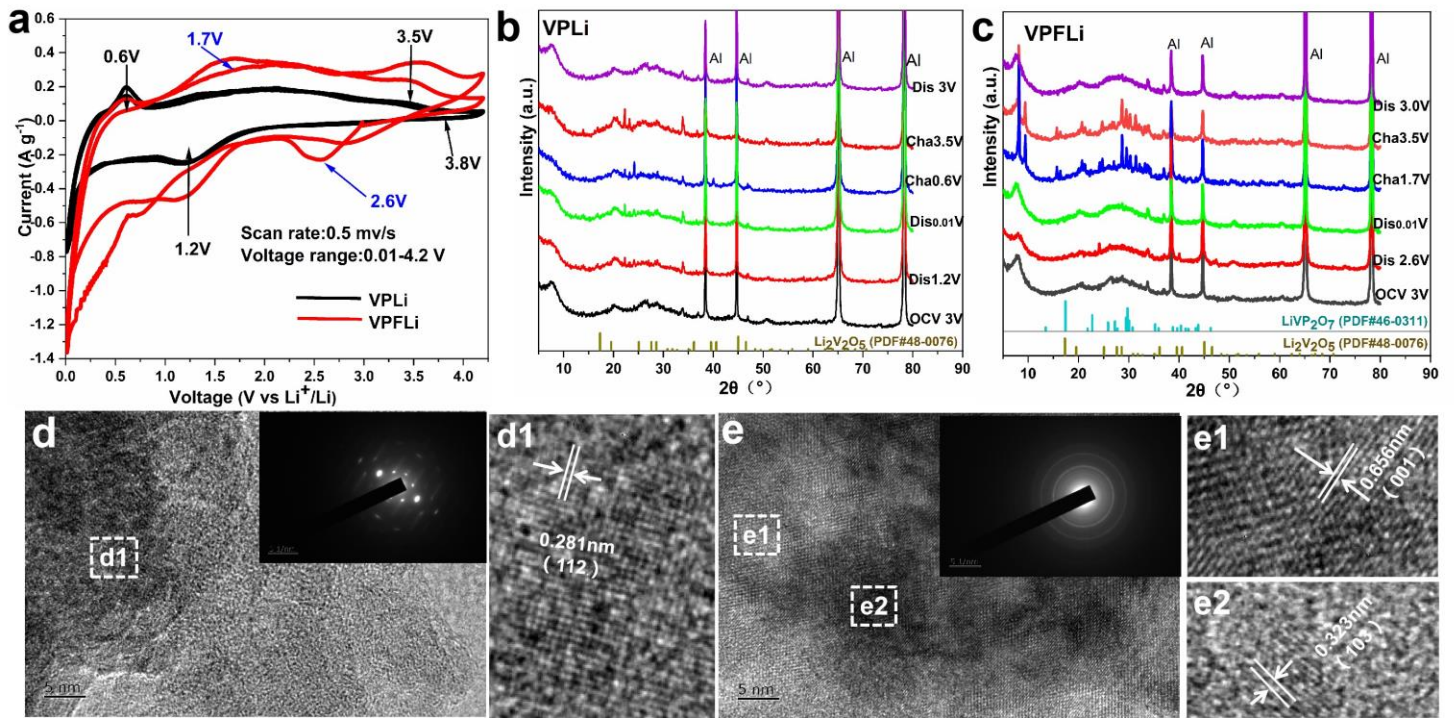


Fig.6. (a) CV curves of VPLi and VPFLi during the first two cycles, (b)-(c) *Ex situ* XRD of VPLi and VPFLi under different charge/ discharge states in the first cycle, (d)-(e) TEM images of VPLi and VPFLi at 3.5 V (charge) in the first cycle (insets: SAED patterns and lattice spacing information).

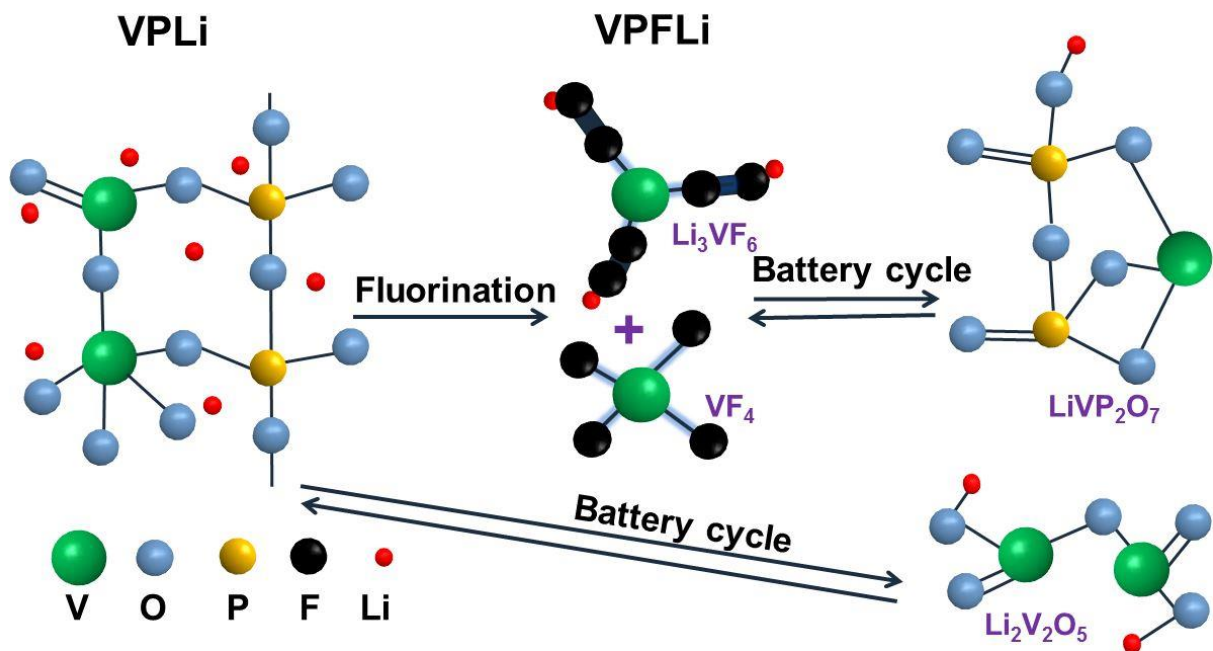


Fig.7. Schematic showing the reaction mechanism during the battery cycles

The presence of nanocrystals within the amorphous glass matrix could lead to a synergistic effect that effectively improve the battery electrical cycle performance [53]. Fluorinated product VPFLi features a polycrystalline structure in which the precipitated  $\text{Li}_3\text{VF}_6$  and  $\text{VF}_4$  nanocrystals were embedded in amorphous phase. Compared to VPLi,  $\text{VF}_4$  and  $\text{Li}_3\text{VF}_6$  crystals were converted into  $\text{LiVP}_2\text{O}_7$  in VPFLi,



296 which led to the increased specific capacity. This is evident by the symmetrical charge/discharge curve and  
297 the improved capacity retention rate. It involves reversible order-disorder transition between crystal and  
298 amorphous phases during the preparation process and charge-discharge cycles.

299 Density functional theory (DFT) based electronic structure calculations for crystalline vanadium-based  
300 electrode materials have been widely reported to date [78.79], and such calculation can reflect the structure  
301 stability, the electrons transfer and the atomic bonding within the materials. However, research into  
302 amorphous materials such as long/short range disordered structures is still in its infancy. The details of the  
303 calculation method based on DFT theoretical model for this study can be found in **Supporting Information**.

304 As shown in Fig.8(a)-(b), the theoretical structural models of VPLi and VPFLi reactants are constructed,  
305 which are  $V_2O_5$  and  $V_2O_{4.5}F_{0.5}$  (molar ratio O/F=9), respectively. Density of states (DOS) is essentially the  
306 number of different states at a specific energy level that electrons are allowed to occupy (the number of  
307 electronic states per unit volume per unit energy). Fig.8(c)-(d) display the total density of states of VPLi and  
308 VPFLi before and after insertion of a single  $Li^+$ . VPLi and VPFLi have semiconductor characteristics with a  
309 large characteristic band gap. After a single Li atom was inserted into VPFLi, its Fermi level moves to the  
310 edge of the conduction band. This indicates a transition into an n-type semiconductor state as the insertion of  
311  $Li^+$  helps reduce the electrical conductivity and electrode impedance of the structure. Fig.8(e)-(f) show the  
312 charge density distribution map of VPLi and VPFLi with a single Li atom insertion, respectively. The  
313 simulation result shows the electronic structure (charge accumulation and depletion) and the chemical  
314 environment of the lattice structure, which is otherwise difficult to measure experimentally. In VPLi, Li  
315 accepts most of the charges transferred from O, while for VPFLi, charges mostly transferred from Li to O  
316 due to the presence of F. Therefore, the substitution of fluorine for oxygen contributes to the improvement  
317 of the electrical conductivity of the structure and the further reduction of the electrode impedance. Since the  
318 battery cycle redox reaction is dependent on reduced oxygen, the reduced irreversible oxygen loss can lead  
319 to the improved cycle stability.

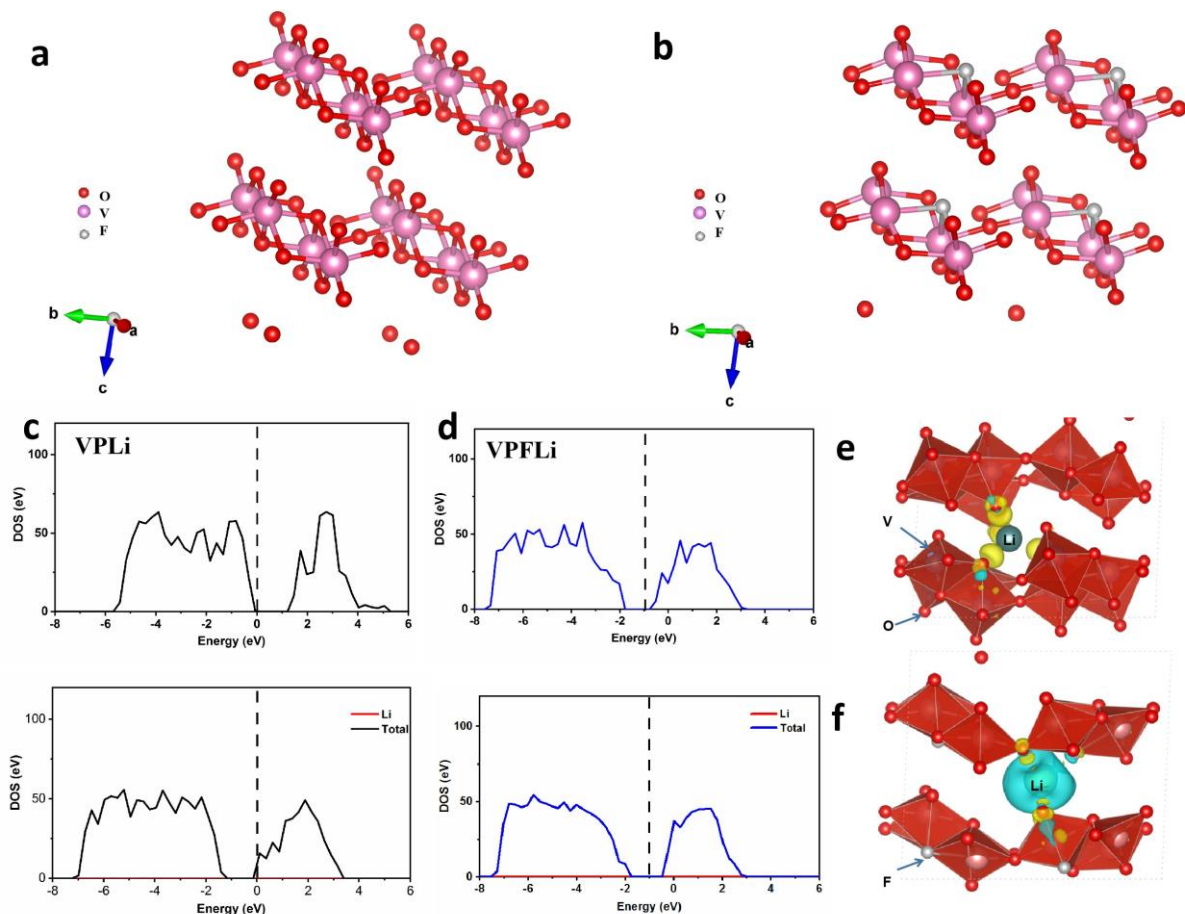


Fig.8. DFT simulation of VPLi and VPFLi for Li ion storage processes. (a)-(b): the theoretical structure models of VPLi and VPFLi, (c)-(d): total density of states of VPLi and VPFLi before and after Li insertion, (e)-(f): charge density difference of VPLi and VPFLi after single Li atom insertion (light blue: charge depletion; yellow: charge accumulation).

## 4. Conclusions

This work presents the first investigation on a fluorinated vanadium-phosphorus amorphous lithium battery cathode material and the associated structure-performance relationship. After fluorination, the  $V^{4+}$  content in the cathode material increased from 16.3% to 23.8%. The fluorinated product VPFLi consists of 10% of precipitates ( $Li_3VF_6$  and  $VF_4$  nanocrystals) and shows an optimal specific capacity of  $344.3 \text{ mAh g}^{-1}$  in the first cycle and  $269.7 \text{ mAh g}^{-1}$  after 200 cycles at a current density of  $50 \text{ mA g}^{-1}$  within a voltage range of 1.5-4.2V. The charge transfer resistance of VPFLi ( $R_{CT} = 704 \Omega$ ) was only half that of VPLi ( $R_{CT} = 1499.7\Omega$ ). Modelling through density functional theory shows that that fluorination contributes to the moving of Fermi level towards the edge of the conduction band, and that charges mostly transferred from Li to O, which led to improved cycle stability.

The lithiation process ( $V^{4+}/V^{5+}$ ) in amorphous VPLi can be related to the conversion of  $V_2O_5$  to  $Li_2V_2O_5$

335 in the cycling process. Compared to VPLi, VF<sub>4</sub> and Li<sub>3</sub>VF<sub>6</sub> crystals were converted into LiVP<sub>2</sub>O<sub>7</sub> in VPFLi,  
336 which increased the specific capacity. It is believed that having VF<sub>4</sub> and Li<sub>3</sub>VF<sub>6</sub> nanocrystals embedded in the  
337 amorphous glass matrix and the associated order-disorder transition between crystal and amorphous phases  
338 can lead to a synergistic effect that enhances the electrical cycle performance of fluorinated  
339 vanadium-phosphorus amorphous cathode in practical lithium ion battery applications. This study provides a  
340 new perspective towards selecting novel cathode material for future lithium-ion batteries.

## 341 **Declarations of interest**

342 The authors declare that they have no known competing financial interests or personal relationships that  
343 could have appeared to influence the work reported in this paper.

## 344 **Acknowledgements**

345 This work was supported by the Natural Science Foundation of Hainan Province (519MS022), the Key  
346 Scientific & Technological Project of Hainan Province (ZDYF2020015), the Research Lab construction of  
347 Hainan University (ZY2019HN09) and the China Scholarship Council under Grant 202107565023.

## 349 **References:**

- 350 [1] T. Sadhasivam, M. Park, J. Shim, J. Jin, S. Kim, M.D. Kurkuri, S. Roh, H. Jung, High charge acceptance through interface  
351 reaction on carbon coated negative electrode for advanced lead-carbon battery system, *ELECTROCHIM. ACTA*, 295(2019)  
352 367-375.
- 353 [2] T. Sadhasivam, G. Palanisamy, S. Roh, M.D. Kurkuri, S.C. Kim, H. Jung, Electro-analytical performance of bifunctional  
354 electrocatalyst materials in unitized regenerative fuel cell system, *INT. J. HYDROGEN ENERG.*, 43(2018) 18169-18184.
- 355 [3] G. Palanisamy, H. Jung, T. Sadhasivam, M.D. Kurkuri, S.C. Kim, S. Roh, A comprehensive review on microbial fuel cell  
356 technologies: Processes, utilization, and advanced developments in electrodes and membranes, *J. CLEAN. PROD.*, 221(2019)  
357 598-621.
- 358 [4] H. Jung, K. Cho, K.A. Sung, W. Kim, M. Kurkuri, J. Park, Sulfonated poly(arylene ether sulfone) as an electrode binder for  
359 direct methanol fuel cell, *ELECTROCHIM. ACTA*, 52(2007) 4916-4921.
- 360 [5] R. Com, Global Energy Harvesting System Market Outlook 2019-2027 - Drivers, Constraints, Opportunities, Threats,  
361 Challenges, Investment Opportunities, 2021.  
362 <https://finance.yahoo.com/news/global-energy-harvesting-system-market-100700710.html>
- 363 [6] G. Lee, Y. Seon Kim, M. Sung, D. Kim, Ultrafine CoP nanoparticles encapsulated in N/P dual-doped carbon cubes derived  
364 from 7,7,8,8-tetracyanoquinodimethane for lithium-ion batteries, *APPL. SURF. SCI.*, 555(2021) 149716.
- 365 [7] K. Zhang, Y. Tian, C. Wei, Y. An, J. Feng, Building stable solid electrolyte interphases (SEI) for micro-sized silicon anode  
366 and 5V-class cathode with salt engineered nonflammable phosphate-based lithium-ion battery electrolyte, *APPL. SURF.*  
367 *SCI.*, 553(2021) 149566.
- 368 [8] C. Zhou, P. Zhang, W. Wang, Y. Yang, W. Wang, H. Ding, X. Xu, W. Ji, L. Chen, Hierarchical modulation of NiSe<sub>2</sub>

- 369 nanosheets/nanodendrites by phase engineering on N-doped 3D porous graphene as self-supporting anode for superior  
370 lithium ion batteries, *APPL. SURF. SCI.*, (2021) 150784.
- 371 [9]M. He, L. Zhang, J. Li, Theoretical investigation on interactions between lithium ions and two-dimensional halide perovskite  
372 for solar-rechargeable batteries, *APPL. SURF. SCI.*, 541(2021) 148509.
- 373 [10]J. Wang, X. Sun, Understanding and recent development of carbon coating on LiFePO<sub>4</sub> cathode materials for lithium-ion  
374 batteries, *ENERG ENVIRON SCI*, 5(2012) 5163-5185.
- 375 [11]S. Neudeck, F. Walther, T. Bergfeldt, C. Suchomski, M. Rohnke, P. Hartmann, J. Janek, T. Brezesinski, Molecular Surface  
376 Modification of NCM622 Cathode Material Using Organophosphates for Improved Li-Ion Battery Full-Cells, *ACS APPL*  
377 *MATER INTER*, 10(2018) 20487-20498.
- 378 [12]W. Oh, H. Park, B. Jin, R. Thangavel, W. Yoon, Understanding the structural phase transitions in lithium vanadium phosphate  
379 cathodes for lithium-ion batteries, *J. MATER CHEM A*, 8(2020) 10331-10336.
- 380 [13]R. Thangavel, K. Kaliyappan, K. Kang, X. Sun, Y.S. Lee, Going Beyond Lithium Hybrid Capacitors: Proposing a New High  
381 - Performing Sodium Hybrid Capacitor System for Next - Generation Hybrid Vehicles Made with Bio - Inspired Activated  
382 Carbon, *ADV ENERGY MATER*, 6(2016) 1502199.
- 383 [14]Y. Subramanian, W. Oh, W. Choi, H. Lee, M. Jeong, R. Thangavel, W. Yoon, Optimizing high voltage Na<sub>3</sub>V<sub>2</sub>(PO<sub>4</sub>)<sub>2</sub>F<sub>3</sub>  
384 cathode for achieving high rate sodium-ion batteries with long cycle life, *CHEM. ENG. J.*, 403(2021) 126291.
- 385 [15]M.S. Whittingham, Lithium Batteries: 50 Years of Advances to Address the Next 20 Years of Climate Issues, *NANO LETT.*,  
386 20(2020) 8435-8437.
- 387 [16]Y. Yue, H. Liang, Micro - and Nano - Structured Vanadium Pentoxide (V<sub>2</sub>O<sub>5</sub>) for Electrodes of Lithium - Ion Batteries,  
388 *ADV ENERGY MATER*, 7(2017) 1602541-1602545.
- 389 [17]X. Xu, F. Xiong, J. Meng, Q. An, L. Mai, Multi-electron reactions of vanadium-based nanomaterials for high-capacity lithium  
390 batteries: challenges and opportunities, *Materials Today Nano*, 10(2020) 100073.
- 391 [18]J. Cao, D. Zhang, Y. Yue, X. Wang, T. Pakornchote, T. Bovornratanaraks, X. Zhang, Z. Wu, J. Qin, Oxygen defect enriched  
392 (NH<sub>4</sub>)<sub>2</sub>V<sub>10</sub>O<sub>25</sub> · 8H<sub>2</sub>O nanosheets for superior aqueous zinc - ion batteries, *NANO ENERGY*, 84(2021) 105876.
- 393 [19]Y. Zhu, M. Yang, Q. Huang, D. Wang, R. Yu, J. Wang, Z. Zheng, D. Wang, V<sub>2</sub>O<sub>5</sub> Textile Cathodes with High Capacity and  
394 Stability for Flexible Lithium - Ion Batteries, *Advanced materials*, 32(2020) 1906205.
- 395 [20]S. Zhang, H. Tan, X. Rui, Y. Yu, Vanadium-Based Materials: Next Generation Electrodes Powering the Battery Revolution?  
396 *ACCOUNTS CHEM. RES.*, (2020) 1660-1671.
- 397 [21]Y. Liu, Z. Sun, X. Sun, Y. Lin, C. Yuan, Construction of ultrathin V<sub>3</sub>S<sub>4</sub>@C nanosheets assembled hierarchical nanotubes  
398 towards alkali on batteries with ion dependent electrochemical mechanisms, *Angewandte Chemie International Edition*,  
399 132(2020) 2494-2503.
- 400 [22]C. Delmas, H. Cognac-Auradou, J.M. Cocciantelli, M. M<sup>é</sup>rier, J.P. Doumerc, The Li<sub>x</sub>V<sub>2</sub>O<sub>5</sub> system: An overview of the  
401 structure modifications induced by the lithium intercalation, *SOLID STATE IONICS*, 69(1994) 257-264.
- 402 [23]Y. Xu, M. Dunwell, L. Fei, E. Fu, Q. Lin, B. Patterson, B. Yuan, S. Deng, P. Andersen, H. Luo, G. Zou, Two-Dimensional  
403 V<sub>2</sub>O<sub>5</sub> Sheet Network as Electrode for Lithium-Ion Batteries, *ACS APPL MATER INTER*, 6(2014) 20408-20413.
- 404 [24]C. Zhang, Z. Chen, Z. Guo, X.W.D. Lou, Additive-free synthesis of 3D porous V<sub>2</sub>O<sub>5</sub> hierarchical microspheres with  
405 enhanced lithium storage properties, *ENERG ENVIRON SCI*, 6(2013) 974-978.
- 406 [25]J. Lee, D.A. Kitchaev, D.H. Kwon, C.W. Lee, J.K. Papp, Y.S. Liu, Z. Lun, R.J. Clement, T. Shi, B.D. McCloskey, Reversible  
407 Mn<sup>2+</sup>/Mn<sup>4+</sup> double redox in lithium-excess cathode materials, *NATURE*, 556(2018) 185-190.
- 408 [26]D.A. Kitchaev, Z. Lun, W.D. Richards, H. Ji, R.J. Cl<sup>é</sup>ment, M. Balasubramanian, D. Kwon, K. Dai, J.K. Papp, T. Lei, B.D.  
409 McCloskey, W. Yang, J. Lee, G. Ceder, Design principles for high transition metal capacity in disordered rocksalt Li-ion  
410 cathodes, *ENERG ENVIRON SCI*, 11(2018) 2159-2171.
- 411 [27]R.J. Cl<sup>é</sup>ment, Z. Lun, G. Ceder, Cation-disordered rocksalt transition metal oxides and oxyfluorides for high energy  
412 lithium-ion cathodes, *ENERG ENVIRON SCI*, 13(2020) 345-373.
- 413 [28]H. Song, M. Luo, A. Wang, High Rate and Stable Li-Ion Insertion in Oxygen-Deficient LiV<sub>3</sub>O<sub>8</sub> Nanosheets as a Cathode  
414 Material for Lithium-Ion Battery, *ACS APPL MATER INTER*, 9(2017) 2875-2882.
- 415 [29]D. Seo, J. Lee, A. Urban, R. Malik, S. Kang, G. Ceder, The structural and chemical origin of the oxygen redox activity in  
416 layered and cation-disordered Li-excess cathode materials, *NAT CHEM*, 8(2016) 692-697.
- 417 [30]L. Du, H. Lin, Z. Ma, Q. Wang, D. Li, Y. Shen, W. Zhang, K. Rui, J. Zhu, W. Huang, Using and recycling V<sub>2</sub>O<sub>5</sub> as high

- 418 performance anode materials for sustainable lithium ion battery, *J. POWER SOURCES*, 424(2019) 158-164.
- 419 [31]Z. Wang, H. Huang, L. Zeng, Y. Wang, D. Fang, In-operando deformation studies on the mechano-electrochemical  
420 mechanism in free-standing MWCNTs/V<sub>2</sub>O<sub>5</sub> lithium ion battery electrode, *ELECTROCHIM. ACTA*, 305(2019) 101-115.
- 421 [32]D. Kong, X. Li, Y. Zhang, X. Hai, B. Wang, X. Qiu, Q. Song, Q. Yang, L. Zhi, Encapsulating V<sub>2</sub>O<sub>5</sub> into carbon nanotubes  
422 enables the synthesis of flexible high-performance lithium ion batteries, *ENERG ENVIRON SCI*, 9(2016) 906-911.
- 423 [33]F. Ye, D. Lu, X. Gui, T. Wang, X. Zhuang, W. Luo, Y. Huang, Atomic layer deposition of core-shell structured V<sub>2</sub>O<sub>5</sub>@CNT  
424 sponge as cathode for potassium ion batteries, *Journal of Materiomics*, 5(2019) 344-349.
- 425 [34]R. Chen, R. Luo, Y. Huang, F. Wu, L. Li, Advanced High Energy Density Secondary Batteries with Multi - Electron  
426 Reaction Materials, *ADV SCI*, 3(2016) 1600051.
- 427 [35]X. Xu, F. Xiong, J. Meng, Q. An, L. Mai, Multi-electron reactions of vanadium-based nanomaterials for high-capacity lithium  
428 batteries: challenges and opportunities, *Materials Today Nano*, (2020) 100073.
- 429 [36]Y. Huang, F. Wu, R. Chen, Thermodynamic analysis and kinetic optimization of high-energy batteries based on  
430 multi-electron reactions, *NATL SCI REV*, 7(2020) 1367-1386.
- 431 [37]Z. Zhou, J. Zhang, S. Chen, H. Yao, Y. Dong, The electrochemical performance and multielectron reaction mechanism of  
432 NiV<sub>2</sub>O<sub>6</sub> as a novel anode material for lithium-ion batteries, *ELECTROCHIM. ACTA*, (2020) 136979.
- 433 [38]H. Song, C. Liu, C. Zhang, G. Cao, Self-doped V<sup>4+</sup> - V<sub>2</sub>O<sub>5</sub> nanoflake for 2 Li-ion intercalation with enhanced rate and  
434 cycling performance, *NANO ENERGY*, 22(2016) 1-10.
- 435 [39]S. Ni, X. Lv, J. Ma, X. Yang, L. Zhang, Electrochemical characteristics of lithium vanadate Li<sub>3</sub>VO<sub>4</sub> as a new sort of anode  
436 material for Li-ion batteries, *J. POWER SOURCES*, 248(2014) 122-129.
- 437 [40]X. Sun, C. Zhou, M. Xie, T. Hu, H. Sun, G. Xin, G. Wang, S.M. George, J. Lian, Amorphous vanadium oxide coating on  
438 graphene by atomic layer deposition for stable high energy lithium ion anodes, *CHEM. COMMUN.*, 50(2014) 10703-10706.
- 439 [41]O.B. Chae, J. Kim, I. Park, H. Jeong, J.H. Ku, J.H. Ryu, K. Kang, S.M. Oh, Reversible Lithium Storage at Highly Populated  
440 Vacant Sites in an Amorphous Vanadium Pentoxide Electrode, *CHEM. MATER.*, 26(2014) 5874-5881.
- 441 [42]J.G. Smith, D.J. Siegel, Low-temperature paddlewheel effect in glassy solid electrolytes, *NAT COMMUN*, 11(2020) 1483.
- 442 [43]R. Garcia Mendez, J.G. Smith, J.C. Neuefeind, D.J. Siegel, J. Sakamoto, Correlating Macro and Atomic Structure with Elastic  
443 Properties and Ionic Transport of Glassy Li<sub>2</sub>S - P<sub>2</sub>S<sub>5</sub> (LPS) Solid Electrolyte for Solid - State Li Metal Batteries, *ADV*  
444 *ENERGY MATER*, 10(2020) 2000335.
- 445 [44]F. Han, A.S. Westover, J. Yue, X. Fan, F. Wang, M. Chi, D.N. Leonard, N.J. Dudney, H. Wang, C. Wang, High electronic  
446 conductivity as the origin of lithium dendrite formation within solid electrolytes, *NAT ENERGY*, 4(2019) 187-196.
- 447 [45]Y. Zhang, Glass anodes for lithium ion batteries: Insight from the structural evolution during discharging/charging, *INT J.*  
448 *APPL GLASS SCI*, 11(2020) 577-589.
- 449 [46]Z. Jiang, T. Zhao, J. Ren, Y. Zhang, Y. Yue, NMR evidence for the charge-discharge induced structural evolution in a Li-ion  
450 battery glass anode and its impact on the electrochemical performances, *NANO ENERGY*, 80(2021) 105589.
- 451 [47]F. Xiong, Q. An, L. Xia, Y. Zhao, L. Mai, H. Tao, Y. Yue, Revealing the atomistic origin of the disorder-enhanced Na-storage  
452 performance in NaFePO<sub>4</sub> battery cathode, *NANO ENERGY*, 57(2019) 608-615.
- 453 [48]M. Du, K. Huang, Y. Guo, Z. Xie, H. Jiang, C. Li, Y. Chen, High specific capacity lithium ion battery cathode material  
454 prepared by synthesizing vanadate - phosphate glass in reducing atmosphere, *J. POWER SOURCES*, 424(2019) 91-99.
- 455 [49]F. Kong, X. Liang, L. Yi, X. Fang, Z. Yin, Y. Wang, R. Zhang, L. Liu, Q. Chen, M. Li, C. Li, H. Jiang, Y. Chen,  
456 Multi-electron reactions for the synthesis of a vanadium-based amorphous material as lithium-ion battery cathode with high  
457 specific capacity, *ENERGY*, 219(2021) 119513.
- 458 [50]T.S. Arthur, K. Kato, J. Germain, J. Guo, P. Glans, Y. Liu, D. Holmes, X. Fan, F. Mizuno, Amorphous V<sub>2</sub>O<sub>5</sub> - P<sub>2</sub>O<sub>5</sub> as  
459 high-voltage cathodes for magnesium batteries, *CHEM. COMMUN.*, 51(2015) 15657-15660.
- 460 [51]S. Afyon, F. Krumeich, C. Mensing, A. Borgschulte, R. Nesper, New High Capacity Cathode Materials for Rechargeable  
461 Li-ion Batteries: Vanadate-Borate Glasses, *SCI REP-UK*, 4(2015) 7113.
- 462 [52]Y. Zhang, P. Wang, G. Li, J. Fan, C. Gao, Z. Wang, Y. Yue, Clarifying the charging induced nucleation in glass anode of  
463 Li-ion batteries and its enhanced performances, *NANO ENERGY*, 57(2018) 592-599.
- 464 [53]Y. Zhang, P. Wang, T. Zheng, D. Li, G. Li, Y. Yue, Enhancing Li-ion battery anode performances via disorder/order  
465 engineering, *NANO ENERGY*, 49(2018) 596-602.
- 466 [54] J. Fan, Y. Zhang, G. Li, Y. Yue, Tellurium nanoparticles enhanced electrochemical performances of TeO<sub>2</sub>-V<sub>2</sub>O<sub>5</sub>-Al<sub>2</sub>O<sub>3</sub>

467 glass anode for Lithium-ion batteries, *J. NON-CRYST. SOLIDS*, 521(2019) 119491.

468 [55]E. Zhao, S. Zhao, X. Wu, J. Li, L. Yu, C. Nan, G. Cao, Electrochemical performance of Li<sub>2</sub>O-V<sub>2</sub>O<sub>5</sub>-SiO<sub>2</sub>-B<sub>2</sub>O<sub>3</sub> glass as  
469 cathode material for lithium ion batteries, *Journal of Materiomics*, 5(2019) 663-669.

470 [56]D. Seo, J. Lee, A. Urban, R. Malik, S. Kang, G. Ceder, The structural and chemical origin of the oxygen redox activity in  
471 layered and cation-disordered Li-excess cathode materials, *NAT CHEM*, 8(2016) 692-697.

472 [57]S. Mandal, S. Hazra, D. Das, A. Ghosh, Structural studies of binary iron vanadate glass, *J. NON-CRYST. SOLIDS*, 183(1995)  
473 315-319.

474 [58]S. Ibrahim, M.A. Marzouk, G.M. El Komy, Structural Characteristics and Electrical Conductivity of Vanadium-doped lithium  
475 Ultraphosphate Glasses, *SILICON-NETH*, 9(2017) 403-410.

476 [59]F. Fu, K. Liao, J. Ma, Z. Cheng, D. Zheng, L. Gao, C. Liu, S. Li, W. Li, How intermolecular interactions influence electronic  
477 absorption spectra: insights from the molecular packing of uracil in condensed phases, *PHYS. CHEM. CHEM. PHYS.*,  
478 21(2019) 4072-4081.

479 [60]W.B. Jensen, The Origin of the Ionic-Radius Ratio Rules, *J. CHEM. EDUC.*, 87(2010) 587-588.

480 [61]L.D. Bogomolova, T.F. Dolgolenko, V.A. Tachkin, V.N. Lazukin, The EPR of V<sup>4+</sup> and Cu<sup>2+</sup> ions as a method of the study  
481 of glass structure, *Journal of Magnetic Resonance* (1969), 15(1974) 283-291.

482 [62]L. Yu, S. Zhao, X. Wu, J. Li, E. Zhao, G. Wei, Lithium ion storage behaviors of (100-x) V<sub>2</sub>O<sub>5</sub>-(x) P<sub>2</sub>O<sub>5</sub> glass as novel anode  
483 materials for lithium ion battery, *J. ALLOY. COMPD*, 810(2019) 151938.

484 [63]P. Nagels, *Electronic transport in amorphous semiconductors*, Springer Berlin Heidelberg, Berlin, Heidelberg, 1985, 113-158.

485 [64]A. Basa, E. Gonzalo, A. Kuhn, F. Garc ía-Alvarado, Facile synthesis of β -Li<sub>3</sub>VF<sub>6</sub>: A new electrochemically active lithium  
486 insertion material, *J. POWER SOURCES*, 207(2012) 160-165.

487 [65]R. Dziembaj, J. Piwowarczyk, Oxygen equilibrium pressure above the V<sub>2</sub>O<sub>5</sub> - x oxide system at 600 °C (x < 0.43), *J. SOLID*  
488 *STATE CHEM.*, 21(1977) 387-392.

489 [66]Z. En-Lai, Z. Shi-Xi, W. Xia, L. Jing-Wei, C. Guozhong, Electrochemical performance of Li<sub>2</sub>O-V<sub>2</sub>O<sub>5</sub>-SiO<sub>2</sub>-B<sub>2</sub>O<sub>3</sub> glass as  
490 cathode material for lithium ion batteries, *Journal of Materiomics*, 5(2019) 663-669.

491 [67]L. Jingwei, Z. Shixi, W. Xia, Y. Lüqiang, Z. Enlai, N. Cewen, Structure and electrochemical properties of C-coated Li<sub>2</sub>O -  
492 V<sub>2</sub>O<sub>5</sub> - P<sub>2</sub>O<sub>5</sub> glass-ceramic as cathode material for lithium-ion batteries, *FUNCT MATER LETT*, 12(2019) 1951002.

493 [68]C. Siu, I.D. Seymour, S. Britto, H. Zhang, J. Rana, J. Feng, F.O. Omenya, H. Zhou, N.A. Chernova, G. Zhou, C.P. Grey, L.F.J.  
494 Piper, M.S. Whittingham, Enabling multi-electron reaction of ε -VOPO<sub>4</sub> to reach theoretical capacity for lithium-ion  
495 batteries, *CHEM. COMMUN.*, 54(2018) 7802-7805.

496 [69]Y.L. Cheah, N. Gupta, S.S. Pramana, V. Aravindan, G. Wee, M. Srinivasan, Morphology, structure and electrochemical  
497 properties of single phase electrospun vanadium pentoxide nanofibers for lithium ion batteries, *J. POWER SOURCES*,  
498 196(2011) 6465-6472.

499 [70]J. Zhu, H. Shen, X. Shi, F. Yang, X. Hu, W. Zhou, H. Yang, M. Gu, Revealing the Chemical and Structural Evolution of  
500 V<sub>2</sub>O<sub>5</sub> Nanoribbons in Lithium-Ion Batteries Using in Situ Transmission Electron Microscopy, *ANAL. CHEM.*, 91(2019)  
501 11055-11062.

502 [71]W. Zhong, J. Huang, S. Liang, J. Liu, Y. Jiang, New Prelithiated V<sub>2</sub>O<sub>5</sub> Superstructure for Lithium-Ion Batteries with Long  
503 Cycle Life and High Power, *ACS ENERGY LETT*, 1(2020) 31-38.

504 [72]A. Pan, H.B. Wu, L. Yu, T. Zhu, X.W.D. Lou, Synthesis of Hierarchical Three-Dimensional Vanadium Oxide  
505 Microstructures as High-Capacity Cathode Materials for Lithium-Ion Batteries, *ACS APPL MATER INTER*, 4(2012)  
506 3874-3879.

507 [73]J.B. Lee, J. Moon, O.B. Chae, J.G. Lee, J.H. Ryu, M. Cho, K. Cho, S.M. Oh, Unusual Conversion-type Lithiation in LiVO<sub>3</sub>  
508 Electrode for Lithium-Ion Batteries, *CHEM. MATER.*, 28(2016) 5314-5320.

509 [74]V. Mani, N. Kalaiselvi, LiVP<sub>2</sub>O<sub>7</sub>/C: A New Insertion Anode Material for High-Rate Lithium-Ion Battery Applications,  
510 *INORG. CHEM.*, 55(2016) 3807-3814.

511 [75]J. Barker, R. Gover, P. Burns, A. Bryan, LiVP<sub>2</sub>O<sub>7</sub>: A viable lithium-ion cathode material? *Electrochemical and Solid State*  
512 *Letters - ELECTROCHEM SOLID STATE LETT*, 8(2005) A446. <https://doi.org/10.1149/1.1979347>

513 [76]K.H. Lii, Y.P. Wang, Y.B. Chen, S.L. Wang, The crystal structure of LiVP<sub>2</sub>O<sub>7</sub>, *J. SOLID STATE CHEM.*, 86(1990)  
514 143-148.

- 515 [77]R. Li, G. Liang, X. Zhu, Q. Fu, Y. Chen, L. Luo, C. Lin, Mo<sub>3</sub>Nb<sub>14</sub>O<sub>44</sub>: A New Li<sup>+</sup> Container for High - Performance  
516 Electrochemical Energy Storage, ENERGY & ENVIRONMENTAL MATERIALS, 4(2021) 65-71.
- 517 [78]T. Wu, K. Zhu, C. Qin, K. Huang, Unraveling the role of structural water in bilayer V<sub>2</sub>O<sub>5</sub> during Zn<sup>2+</sup> intercalation: insights  
518 from DFT calculations, J. MATER CHEM A, 7(2019) 5612-5620.
- 519 [79]A. Xu, L. Shi, L. Zeng, T.S. Zhao, First-principle investigations of nitrogen-, boron-, phosphorus-doped graphite electrodes  
520 for vanadium redox flow batteries, ELECTROCHIM. ACTA, 300(2019) 389-395.

521